Hindawi
Structural Control and Health Monitoring
Volume 2024, Article ID 9988034, 18 pages
https://doi.org/10.1155/2024/9988034

WILEY | Hindawi

Research Article

A Novel SMFL-Based Assessment Method for Corrosion Nonuniformity of Rebar and Its Application in Reliability Analysis of Corroded RC Beam

Junli Qiu,[1,2] **Yue Jing**,[1,2] **Weiping Zhang**,[1,2] **and Chao Jiang**[1,2]

[1]*Key Laboratory of Performance Evolution and Control for Engineering Structures of Ministry of Education, Tongji University, 1239 Siping Road, Shanghai 200092, China*
[2]*Department of Structural Engineering, Tongji University, 1239 Siping Road, Shanghai 200092, China*

Correspondence should be addressed to Weiping Zhang; weiping_zh@tongji.edu.cn

Received 6 November 2023; Revised 7 February 2024; Accepted 24 February 2024; Published 13 March 2024

Academic Editor: Francesc Pozo

The reliability of corroded reinforced concrete (RC) structures relies on the accurate minimum cross-sectional area of corroded rebar. In this study, the accurate morphologies and self-magnetic flux leakage (SMFL) field strengths of twenty-eight non-uniformly corroded rebars were obtained using 3D structural light scanning and micromagnetic detection technologies, based on which three indices of the SMFL field variation ratio dH, the corrosion non-uniformity degree dS_n, and the cross-sectional area ratio $K_{0.25}$ are proposed. The statistical results show that the probability densities of dS_n and $K_{0.25}$ obey the Weibull distribution and Gamma distribution at the 95% confidence level, respectively, and their distribution parameters are linearly or inversely proportional to dH. The probability density distribution of the minimum cross-sectional area of corroded rebar can be determined using indices dS_n and $K_{0.25}$, based on which a feasible SMFL-based reliability assessment method of corroded RC structures is proposed. The case study of a real specific corroded RC beam shows that the reliability assessment error of the SMFL-based method is only 1.2%, which is much lower than the 20.7% error of the existing method. This SMFL-based method provides a novel idea that can automatically and accurately assess the effect of rebars' corrosion non-uniformity on the reliability of specific in-serviceRC structures.

1. Introduction

Reinforced concrete (RC) structures commonly used in civil infrastructure face long-term adverse effects from the complex environment, such as chloride ion attack, sulfate ion attack, and carbonation, resulting in the developing corrosion of the embedded rebars [1–5]. Corrosion of rebars brings many negative consequences, one of which is the substantially reduced reliability of RC structures [6, 7].

Many reliability assessment methods for RC structures have been developed, such as the out-crossing rate method [8], the first-order and second-order methods [9, 10], the probability density evolution method [11, 12], and the novel adaptive method for the small-failure probability analysis [13]. However, these well-developed methods confronted difficulties in establishing and solving complex mathematical models, for which the Monte Carlo simulation (MCS) to approximate failure probability by failure frequency of a large number of simulations is an effective alternative solution [14–16]. When the rebar's average cross-sectional area is known, the accuracy of MCS depends largely on the assessment accuracy of the minimum cross-sectional area of corroded rebars and the negligence of longitudinal corrosion non-uniformity leads to an unacceptable misestimation of structural reliability [14, 17]. To solve this problem, our group have proposed a cross-sectional area spatial heterogeneity factor R (ratio of the average and minimum cross-sectional areas), based on which the effect of corrosion non-uniformity on the reliability of RC beams is successfully considered [17–19].

However, the existing probability density distribution (PDD) model of factor R is a predictive model based on the statistical analysis of the cross-sectional area data of artificially corroded rebar samples [17, 20, 21], which is not comprehensive enough and may not be suitable to describe the random corrosion non-uniformity of rebars in a specific in-service RC structure. Generally, the corrosion of rebars has a strong randomness closely related to environmental factors, material properties, and structural stress. Chloride ion attack and concrete carbonization are two main reasons that lead to the corrosion of rebars, directly influencing the initiation time of reinforcement corrosion. The transport of chloride ions in concrete is a stochastic process that substantially depends on the mix composition and binder addition of concrete, surface chloride concentration, temperature, and relative humidity in the surrounding environment [3, 22–25]. Concrete carbonation is also a stochastic process affected by the concrete itself and environmental conditions [4, 26–28]. In addition, both of them will be accelerated by stress-induced cracks [26, 29–31], resulting in more significant non-uniform corrosion morphology [32].

With the help of detection or monitoring information, the actual reliability and service status of the RC structures can be assessed more accurately [33, 34]. The non-uniform corrosion defect of the ferromagnetic rebar causes a self-magnetic flux leakage (SMFL) field variation, which can be accurately detected or monitored with high-precision micromagnetic sensors [35–43]. Our group and some other researchers have confirmed the good linear correlation between corrosion degree and the corrosion-induced SMFL field variation amplitude [38–41]. Experimental studies and engineering applications have shown that the SMFL field variation can characterize the exact corrosion defects of rebars non-destructively and conveniently, and have nothing to do with the random development process of non-uniform corrosion [37, 42, 43]. For the issue of magnetization state difference of rebars, some solutions have been proposed, and applicable SMFL-based nondestructive quantitative methods for the corrosion degree of rebars have been established by our group [43–45]. These results show that the SMFL-based characterization of the non-uniform corrosion of rebars is a good choice to avoid the trouble of the stochastic corrosion process and the extensive statistical work of establishing the PDD model for factor R.

In this study, the accurate morphologies and SMFL field strength data of twenty-eight non-uniformly corroded rebars were acquired using 3D structural light scanning and micro-magnetic detection technologies. The SMFL-based assessment of the minimum cross-sectional area of corroded rebar is realized, based on which the effect of corrosion non-uniformity on the reliability of the corroded RC beam is explored.

2. Concepts

As shown in Figure 1, the reliability index β of a corroded RC beam can be calculated using the MCS method with the following four steps [17, 18, 46]. First, the corroded RC beam is divided into a series system consisting of s beam segments with the same length (for example, 100 mm). Second, the PDDs of the load, material strength, cross-sectional sizes, and rebar's minimum cross-sectional area $S_{\min}$ of the corroded RC beam are determined, based on which a set of values for them are randomly sampled. Third, the ultimate flexural bearing capacity M_u and applied bending moment M_S of all beam segments are calculated according to this set of values. In the i-th simulation, the corroded RC beam is regarded to fail once the M_S of any segment exceeds its M_u, and the failure number $n_{f-i} = 1$. Fourth, the probability of an event is estimated with the frequency of the incident in N times of simulation, for example, $N = 1000000$. The estimation value failure probability p_f is

$$p_f = \frac{N_f}{N} = \frac{1}{N}\sum_{i=1}^{N} n_{f-i}. \tag{1}$$

Then, the reliability index β is

$$\beta = -\Phi^{-1}(p_f). \tag{2}$$

The $S_{\min}$ is a key part of the MCS-based reliability assessment procedure of the corroded RC beam. Generally, only the average corrosion degree of rebars can be obtained using theoretical prediction, non-destructive monitoring, and destructive detection [47–49], based on which the rebar's average cross-sectional area S_{avc} can be obtained. However, as shown in Figure 1, the minimum cross-sectional area $S_{\min}$ of a certain segment with a width of 100 mm of an actual corroded rebar is significantly smaller than S_{avc}. Using $S_{\min}$ instead of S_{avc} in the reliability assessment of corroded RC beams avoids errors of up to 200% [14], and thus how to accurately assess $S_{\min}$ when S_{avc} is known is a problem.

As shown in Figure 1(a), method 1 to solve this problem is to use the Gumbel PDD of the cross-sectional area spatial heterogeneity factor R [17, 20, 21]. According to this Gumbel distribution, s values of R used to calculate the $S_{\min}$ for the s beam segments can be randomly sampled in each simulation of MCS. However, as mentioned before, these R values are predictive results based on experimental data [17, 20, 21], which may not be suitable for a specific in-service RC structure.

Therefore, SMFL-based method 2 for assessing the $S_{\min}$ is proposed. The SMFL non-destructive detection has a good capability to assess the actual random corrosion degree of a specific in-service RC beam. As shown in Figure 1(b), the commonly used rebars are usually longitudinally (x-axis) magnetized under the actions of hot rolling and tension, that is, the minor components V_y and V_z of the magnetization vector $\mathbf{V}$ can be ignored compared to the major component V_x [44, 50]. For rebar that has a local V-shape corrosion defect with a width of $2w$ and a depth of d, the magnetization component V_x leads to a steady-state magnetic charge distribution on the circumferential ridge lines at both ends of the corrosion defect with a density of $\pm\rho = \pm 0.5V_x \cdot d$[44]. According to Coulomb's law of magnetism, the components H_x and H_z of the SMFL field strength vector $\mathbf{H}$ generated by the magnetic charges $\pm\rho$ at a spatial point P (x, y, z) are as follows [44]:

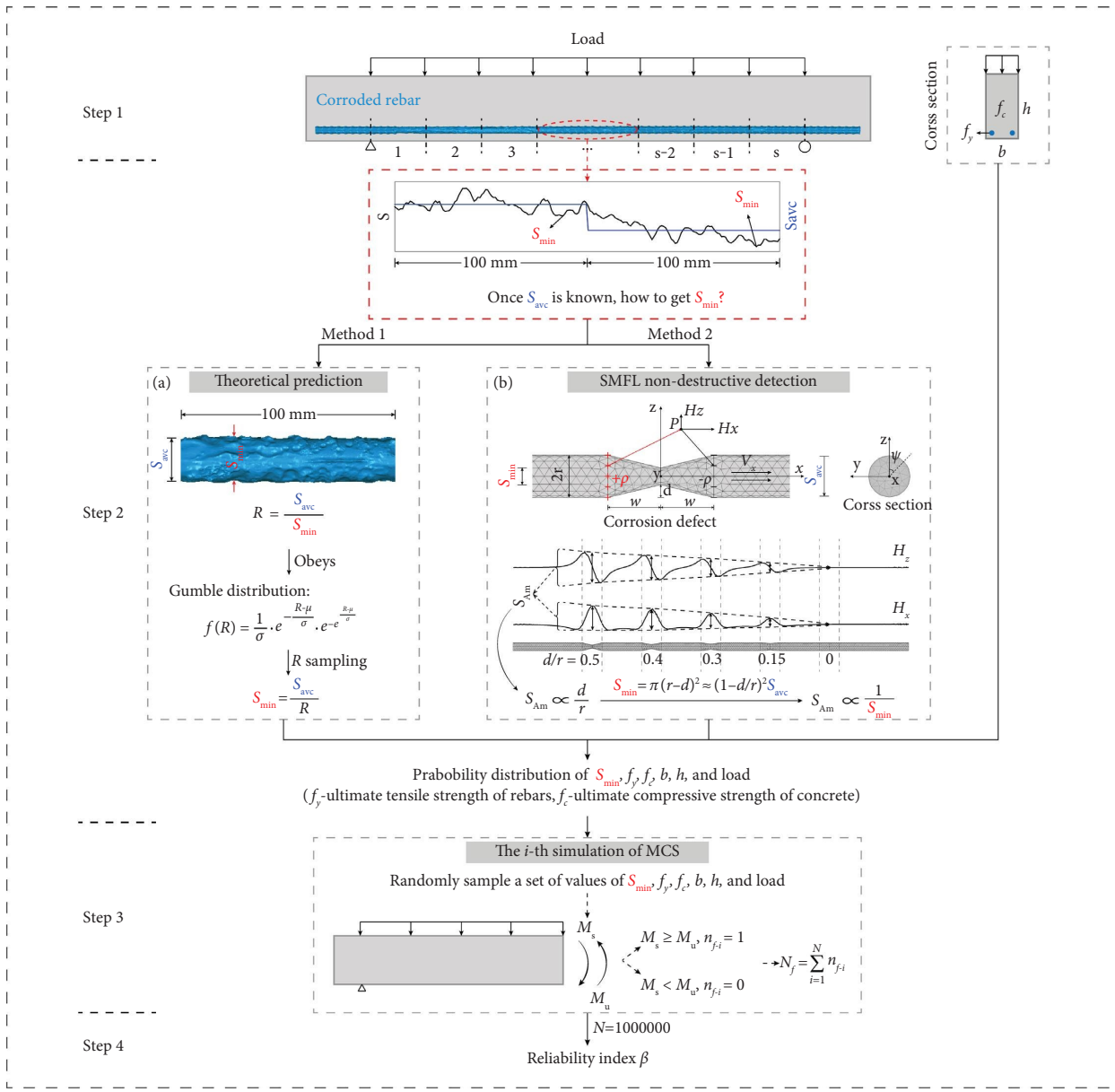

Figure 1: The MCS-based calculation process of β of corroded RC beam based on (a) factor R and (b) SMFL field variation.

$$\begin{cases} H_x = \dfrac{\mathrm{d}r V_x}{8\pi\mu_0} \displaystyle\sum_{i=1,2} \int_0^{2\pi} \frac{(-1)^i \left[x + (-1)^i w\right] \mathrm{d}\varphi}{\left[x + (-1)^i w\right]^2 + (y - r\sin\varphi)^2 + (z - r\sin\varphi)^2} = \frac{\mathrm{d}V_x}{8\pi\mu_0} f_1(x, y, z, w, r), \\ H_z = \dfrac{\mathrm{d}r V_x}{8\pi\mu_0} \displaystyle\sum_{i=1,2} \int_0^{2\pi} \frac{(z - r\sin\varphi) \mathrm{d}\varphi}{\left[x + (-1)^i w\right]^2 + (y - r\sin\varphi)^2 + (z - r\sin\varphi)^2} = \frac{\mathrm{d}V_x}{8\pi\mu_0} f_2(x, y, z, w, r), \end{cases} \tag{3}$$

where r is the radius of the rebar, $\mu_0 = 4\pi \times 10^{-7}$ H/m is the vacuum magnetic permeability, and $f_1(\cdot)$ and $f_2(\cdot)$ are functions of x, y, z, w, and r.

Based on equation (3), set $V_x = 1000$ A/m, $y = 0$, $z = 30$ mm, $w = 25$ mm, $r = 5$ mm, and then the numerical solutions (see Figure 2(d) for calculating flow) of H_x and H_z of five local V-shape corrosion defects with the maximum relative corrosion depths d/r of 0.5, 0.4, 0.3, 0.15, and 0 are shown in Figure 1(b). The corrosion defects cause local variations in the H_x and H_z curves, and the variation amplitudes S_{Am} are proved to be positively linearly correlated with d/r [38–41]. Since S_{Am} is positively correlated with d/r and is negatively correlated with

S_{min} when S_{avc} is known. Therefore, the corrosion-induced SMFL field variation has great potential to assess the S_{min} of corroded rebar.

Different from the R-based prediction of S_{min}, the SMFL-based non-destructive assessment obtains the real S_{min} of corroded rebars, which is practical and widely applicable to the reliability assessment of specific in-service RC structures.

3. Experiment and Finite Element Modeling Details

The experiment and finite element modeling processes are shown in Figure 2, which is described in detail in our previous work [51]. As shown in Figure 2(a), the twenty-two naturally corroded rebar specimens S-NC-1 – S-NC-22 were taken out from the longitudinal girder of a wharf bridge that naturally corroded in the marine environment for twenty-six years, and six artificially corroded specimens S-AC-1 - S-AC-6 were obtained by corroding uncorroded rebars taken out of this girder using the impressed current method. The impressed current corrosion of specimens S-AC-1 - S-AC-6 aimed to create random corrosion morphology with different corrosion degrees similar to naturally corroded rebars. Therefore, we did not set a target corrosion degree and these six rebars were corroded with a constant corrosion current density but random corrosion duration.

As shown in Figure 2(b), the 3D structural light scanning with an accuracy of up to 0.02 mm was employed to capture precise corrosion morphologies of all the rebar specimens. On this basis, the accurate actual corrosion degrees for every cross-section of each rebar specimen can be obtained.

The TSC-7M-16 device was then used to collect the SMFL field variation data of the rebar specimens, as shown in Figure 2(c). Five longitudinal SMFL scanning paths directly above the corroded rebar specimen were conducted at different lift-off heights (LFH) of 5, 10, 30, 50, and 100 mm. Along these paths, four micromagnetic sensors (1#–4#) and a displacement pedometer mounted on the small trolley were utilized to measure the SMFL strength and corresponding measurement location with an accuracy of 0.1 A/m and 1 mm, respectively. The measured data was recorded by the host and transmitted to a computer for further analysis. For brevity, only SMFL strength data measured by micromagnetic sensor 2# was employed in this study.

Since the complex corrosion morphologies of corroded rebar specimens, the analytical solution of its SMFL field according to equation (3) is not feasible. Therefore, the finite element simulation was carried out using the COMSOL^{R} software (COMSOL Inc, Stockholm, Sweden), whose simulation flow is shown in Figure 2(d). In the simulation, the real entity model of the rebar specimen obtained by structured light scanning was inputted. A cuboid air domain was created with the corroded rebar serving as the center, and the boundary condition of the air domain was then set to the external magnetic flux density. The relative magnetic permeability μ_{rs} and μ_{ra} of the rebar and air domain were set to 200 and 1.0 [51], respectively, where μ_{rs} is closely related to the magnetization induced by geomagnetic field $\mathbf{H_e}$:

$$\mathbf{V_h} = (\mu_{rs} - \mu_{ra})\mathbf{H_e}, \tag{4}$$

where $\mathbf{V_h}$ is the magnetization vector induced by $\mathbf{H_e}$.

In Figure 2(d), the components H_{ex}, H_{ey}, and H_{ez} of $\mathbf{H_e}$ were measured values. The rebar's magnetization vector $\mathbf{V} = \mathbf{V_h} + \mathbf{V_r}$, where $\mathbf{V_r}$ was the residual longitudinal linear magnetization vector of the rebar generated by manufacturing and tension. According to the ideal longitudinal magnetization hypothesis, the components of $\mathbf{V_r}$ was set as $V_{rx} = (a \cdot x + b)$ T, $V_{ry} = 0$, and $V_{rz} = 0$, where a and b were adjusted to the suitable values according to the measured SMFL strength. Consequently, the finite element model was ultra-finely meshed using free tetrahedron and then solved. When using the default ultra-refinement meshing setting, the solution converged rapidly, typically within 50 iterations or fewer. Thereby, the finite element simulation of the in-service condition of the SMFL field of bare corroded rebar in Figure 2(c) was realized.

4. Results and Discussion

4.1. Cross-Sectional Area and SMFL Field Variation of Corroded Rebars. For brevity, the naturally and artificially corroded specimens S-NC-8 and S-AC-1 are taken as examples to demonstrate features of the corrosion-induced cross-sectional area S and SMFL field components H_x and H_z, as shown in Figures 3(a) and 3(b) [51]. The S curves are actual ones measured from the rebars' entity models, whose fluctuations and spikes are induced by the corrosion non-uniformity and cathodic protection of stirrups [52], respectively. The features of both the experimental and simulated H_x and H_z induced by natural and artificial corrosion are almost the same, whose fluctuations represent the SMFL field variation caused by the non-uniform corrosion morphology of the corroded rebar. This result shows that the theoretical analysis in Figure 1(b) is established in actual situations. However, the H_x and H_z curves only reveal limited information on non-uniform corrosion and cannot be used to characterize S_{min}.

In this study, both the measured and simulated H_x and H_z curves were stepped. However, to facilitate further analysis, the H_x and H_z curves must be smoothed. To this end, we utilized the Savitzky-Golay (SG) smoothing [53] and Adjacent-Average (AAv) smoothing [54]. The SG smoothing is also called polynomial smoothing, with two control parameters of n and m. The parameter n determines the degree of polynomial fitting and the parameter m determines the amount of data involved in the SG smoothing. Given that secondary fitting sufficed, the parameter n was set as 2. It is important to note that increasing m would result in a larger difference between the SG smoothed H_x value and the original H_x value, leading to the loss of SMFL field variation information [51]. Consequently, we chose a relatively small value of 5 for the parameter m.

For theoretical description, the finite element modeling of rebar has five local V-shape corrosion defects with maximum relative corrosion depth d/r of 0.2, 0.1, 0.07, 0.05, and 0.03 as shown in Figure 3(c) was carried out according to Figure 2(d). Based on the simulated data of H_x, the real

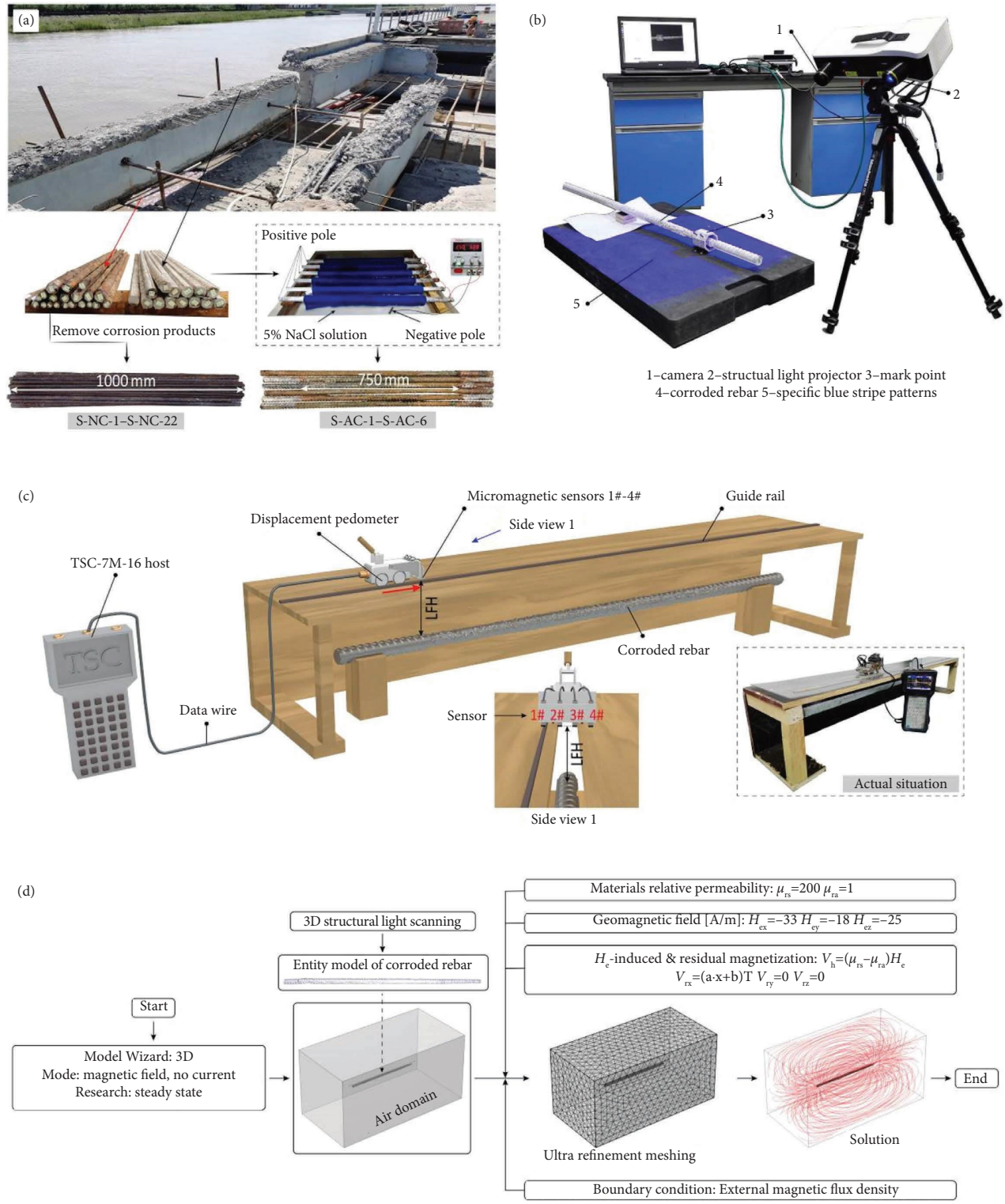

FIGURE 2: (a) Acquisition and processing of corroded rebar specimens, (b) 3D structural light scanning, (c) SMFL field variation scanning, and (d) finite element modeling flow [51].

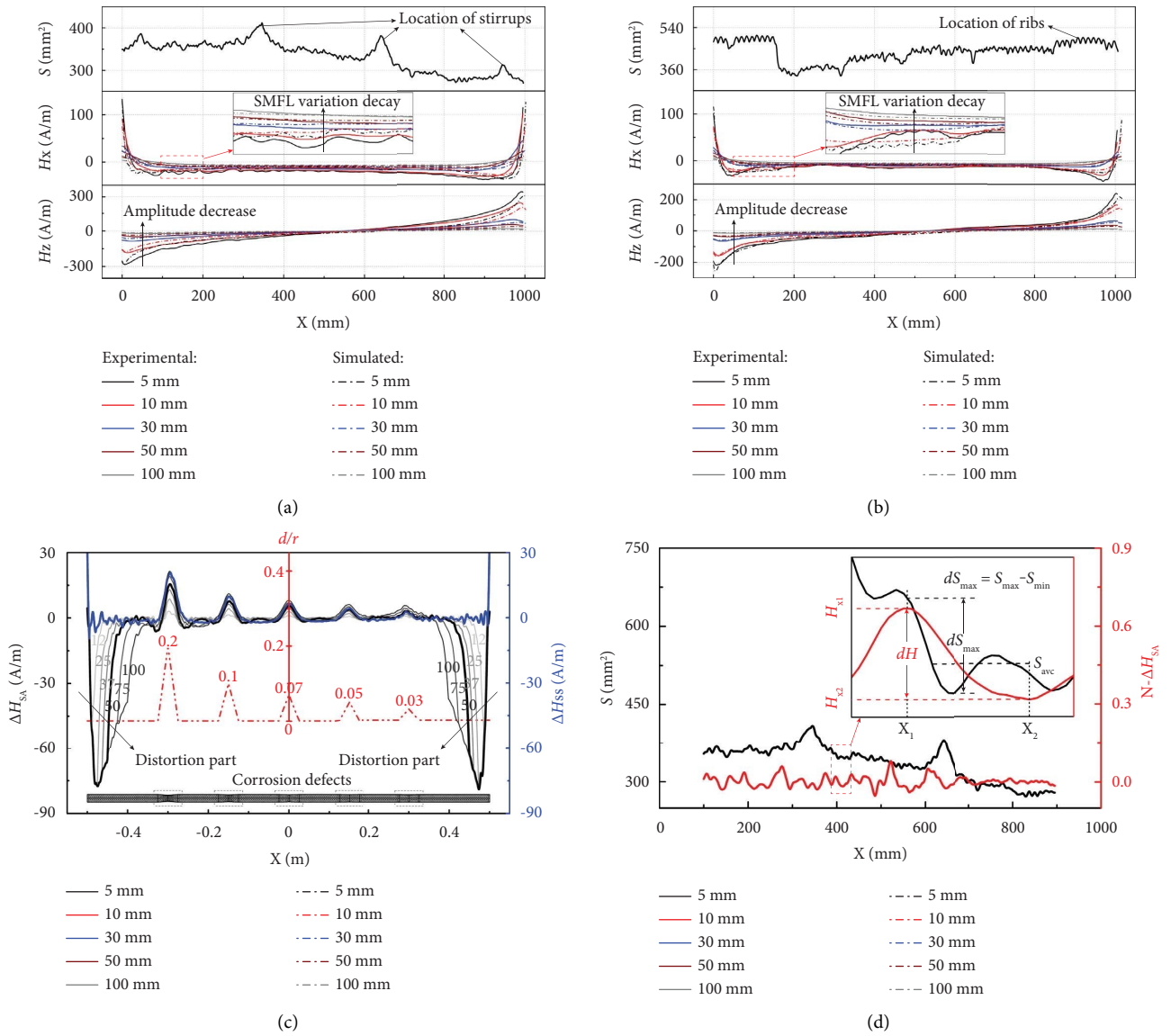

FIGURE 3: Cross-sectional area S and SMFL field components $H_x$and H_z of specimens (a) S-EC-8 and (b) S-AC-1, (c) finite element modeling-based real SMFL field variation ΔH_{SS} and simulated SMFL field variation ΔH_{SA}, and (d) definitions of indices dH, dS_n [51], and K.

and simulated SMFL field variations ΔH_{SS} and ΔH_{SA} are respectively defined as follows:

$$\begin{cases} \Delta H_{SS} = [H_x]_{SG} - [H_{x-S}]_{SG}, \\ \Delta H_{SA} = [H_x]_{SG} - [H_x]_{AAv}, \end{cases} \tag{5}$$

where $[H_x]_{SG}$ and $[H_{x-S}]_{SG}$ are the SG smoothing results ($n = 2$ and $m = 5$) of the simulated H_x of the V-shape corroded rebar in Figure 3(c) and its corresponding smooth uncorroded rebar, respectively, and $[H_x]_{AAv}$ is the AAv smoothing results of the simulated H_x of the V-shape corroded rebar.

When there is only the SMFL detection data of corroded rebars, only ΔH_{SA} can be obtained while ΔH_{SS} cannot. The ΔH_{SS} and ΔH_{SA} curves are shown in Figure 3(c), where the numbers on the ΔH_{SA} curves are the value of AAv smoothing parameter m. It can be seen that the ΔH_{SA} curve with $m = 50$ agrees with the ΔH_{SS} curve better, especially when corrosion degree $d/r \le 0.1$. The ΔH_{SA} curve with smaller d/r deviates significantly from the ΔH_{SS} curve when $m > 50$. In addition, the ΔH_{SA} curve with a larger m has a larger distortion part that means more data loss. Therefore, the ΔH_{SA} curve with $m = 50$ is the best choice to characterize the real SMFL field variation ΔH_{SS} when there is only the SMFL detection data of corroded rebars. Accordingly, based on the principle of eliminating the difference in residual magnetization $\mathbf{V_r}$ of rebars [44], the quantitative SMFL variation degree N-ΔH_{SA} is defined as follows:

$$\text{N-}\Delta H_{SA}[i] = \frac{\Delta H_{SA}[i]}{H[i]} = \frac{\Delta H_{SA}[i]}{\sqrt{H_x[i]^2 + H_z[i]^2}}, \quad i \in [0, L], \tag{6}$$

where $H[i]$ is the total SMFL field strength and L (units: mm) is the rebar's length.

The N-ΔH_{SA} curve of specimen S-NC-8 is shown in Figure 3(d), which quantitatively and intuitively reflects the SMFL field variation induced by the changing cross-sectional area S compared with the original results in Figures 3(a) and 3(b). According to Figure 3(d), three indices SMFL field variation ratio dH, the corrosion non-uniformity degree dS_n [51], and the cross-sectional area ratio K are defined as follows:

$$\begin{cases} \mathrm{dH} = \left|\left(\text{N-}\Delta H_{\mathrm{SA}}\right)_{\mathrm{X1}} - \left(\text{N-}\Delta H_{\mathrm{SA}}\right)_{\mathrm{X2}}\right|, \\ \mathrm{dS_n} = \dfrac{\mathrm{dS_{max}}}{S_{\mathrm{avc}}} = \dfrac{S_{\mathrm{max}} - S_{\mathrm{min}}}{S_{\mathrm{avc}}}, \\ K = \dfrac{S_{\mathrm{max}} - S_{\mathrm{avc}}}{S_{\mathrm{avc}} - S_{\mathrm{min}}}, \end{cases} \tag{7}$$

where subscripts X_1 and X_2 are the abscissas of any two adjacent extreme values on the N-ΔH_{SA} curve, and S_{max}, S_{avc}, and S_{min} are the maximum, average, and minimum cross-sectional areas within the interval $[X_1, X_2]$.

Using the N-ΔH_{SA} and S curves of each specimen, data of dH and the corresponding dS_n and K can be obtained, which satisfies the

$$S_{\mathrm{min}} = \left[1 - \frac{\mathrm{dS}_n}{K+1}\right] \bullet S_{\mathrm{avc}}. \tag{8}$$

Therefore, the SMFL-based idea of obtaining S_{min} when S_{avc} is known in Figure 1(b) can be realized based on indices K and dS_n that are characterized according to the SMFL field variation ratio dH.

4.2. SMFL-Based PDDs of dS_n and K

4.2.1. Results and PDD Estimation Method of dS_n and K. According to the definitions in equation (7) and the N-ΔH_{SA} curves of all the specimens, dH and its corresponding dS_n [51] and K are obtained as shown in Figure 4. As shown in Figure 4(a), when LFH ≤30 mm, the experimental dS_n is well linearly correlated with dH with a fitted slope of about 1.0. When LFH >30 mm, this linear correlation is no longer good due to the decay and mutual interference of the SMFL field originating from different adjacent corrosion defects. The simulated dS_n and dH have linear relationships similar to the experiment results, which adequately reveals that the corrosion-induced cross-sectional area loss causes an equal-proportional magnetic flux leakage of the rebar. Both experimental and simulated data points of dS_n show large discreteness with an increasing trend as the increase of LFH. As shown in Figure 4(b), both the experimental and simulated K are distributed in the interval [0.25, 4.0], which does not apparently change with the increasing LFH. To describe the distribution characteristics of dS_n and K more accurately, statistical analysis is further implemented. The reliability of the measured SMFL data was verified through the consistency observed between simulation results and experimental results. Building upon this foundation, further analysis was performed using the experimental data depicted in Figure 4.

The statistical analysis of dS_n and K are based on the nonparametric kernel density estimation (KDE) method [55, 56], which fits the PDD exactly based on the samples instead of certain precedent probability hypotheses. Suppose a set of samples $x_1, x_2, x_3, \ldots, x_t$ obeys an unknown continuous distribution $p(x)$, then the kernel density estimation at any point x is defined as follows:

$$\widehat{p}(x,h) = \frac{1}{t}\sum_{i=1}^{t} K_h(x - x_i), \tag{9}$$

where $K_h(\bullet)$ is the kernel function, and h is the bandwidth.

$K_h(\bullet)$ satisfies the definition of the probability density function and has many forms, where the Gaussian kernel function (standard normal distribution function) is employed:

$$N(x) = \frac{1}{\sqrt{2\pi}}\exp\left(-\frac{x^2}{2}\right). \tag{10}$$

The bandwidth h affects the relative weight of each sample by changing the independent variable value of $K_h(\bullet)$:

$$K_h(x) = \frac{1}{h}N\left(\frac{x}{h}\right). \tag{11}$$

Substituting equations (11) into (9) to get

$$\widehat{p}(x,h) = \frac{1}{th}\sum_{i=1}^{n} N\left(\frac{x - x_i}{h}\right). \tag{12}$$

The bandwidth h can be optimized to minimize the estimation error (generally the mean integral square error (MISE)) of the KDE method. The MISE is defined as follows:

$$\mathrm{MISE}(h) = E\int [\widehat{p}(x,h) - p(x)]^2 \mathrm{dx}. \tag{13}$$

With the weak assumptions:

$$\mathrm{MISE}(h) = \frac{\int N(x)^2 \mathrm{dx}}{\mathrm{th}} + \frac{1}{4}\left[\int x^2 N(x)\mathrm{dx}\right]^2 h^4 \int p''(x)^2 \mathrm{dx} + o\left(\frac{1}{\mathrm{th}} + h^4\right). \tag{14}$$

There is an optimal bandwidth h_{opt} that minimizes MISE(h):

$$h_{\mathrm{opt}} = \left(\frac{\int K(x)^2 \mathrm{dx}}{t\left[\int x^2 K(x)\mathrm{dx}\right]^2 \int p''(x)^2 \mathrm{dx}}\right)^{1/5} \sim t^{1/5}. \tag{15}$$

In this study, this optimal bandwidth h_{opt} is used.

4.2.2. SMFL-Based PDD of Index dS_n. Based on the KDE method and the samples in Figure 4(a), the true PDD of dS_n can be obtained. According to Figure 4(a), the distribution of

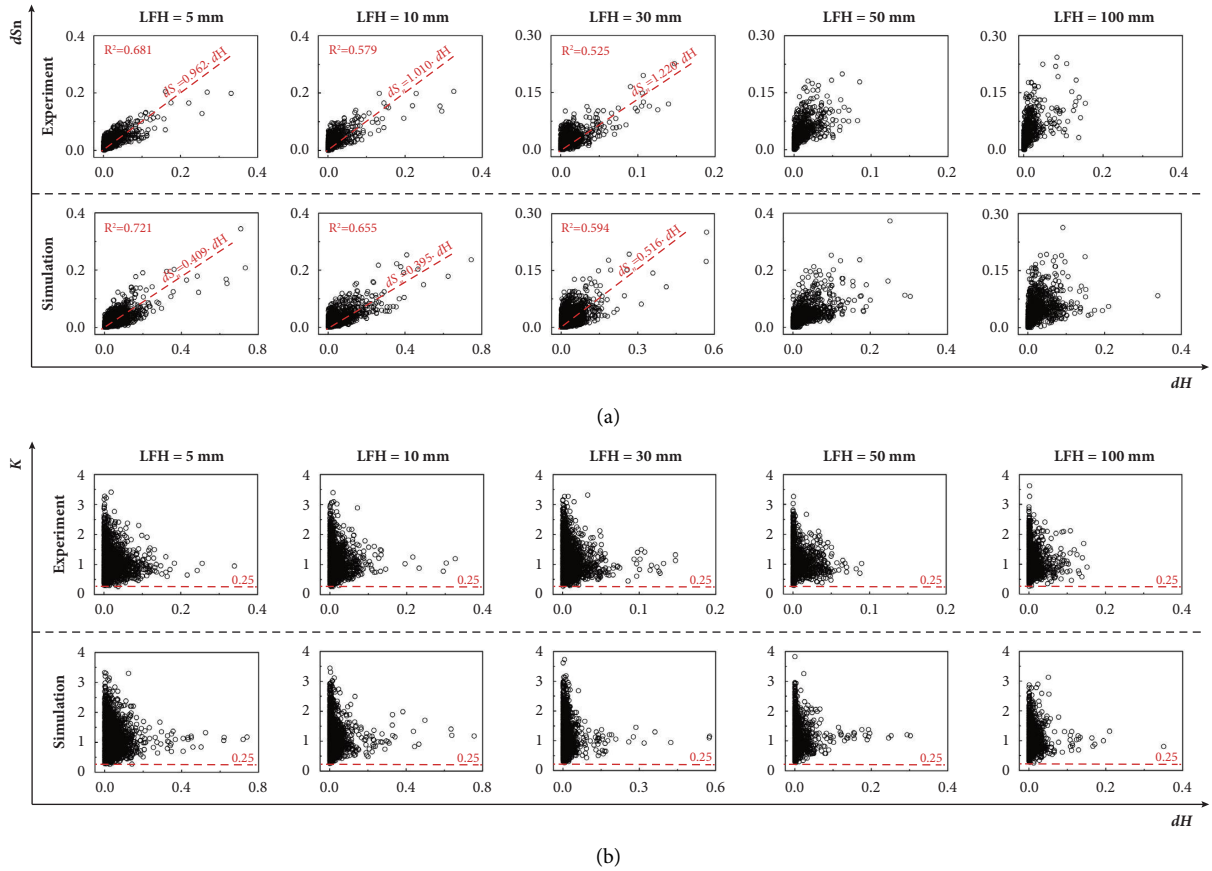

Figure 4: Scatter plots of experimental and simulated indices. (a) dS_n [51] and (b) K with different LFH.

dS_n samples is affected by the increasing LFH. Considering that the concrete cover thickness of the common RC structure is generally no more than 30 mm, and thus the dS_n sample (2923 data points) with LFH = 30 mm is estimated first. As shown in Figure 5, when LFH = 30 mm, 97.4% of dS_n data points are in the interval $dH = [0, 0.03]$, while only 2.6% are in the interval $dH = [0.03, 0.15]$. To ensure the data volume for statistical analysis, the dH interval [0, 0.03] is equally divided into ten intervals while the interval [0.03, 0.15] is not divided, and the mean value of dH in each interval is represented by dH_{av}.

The KDE results of dS_n for the eleven dH intervals are shown in Figures 6(a)–6(k), which exactly reflects the true PDDs of dS_n represented by the histograms. The two-dimensional PDD of dS_n shown in Figure 6(m) is obtained by merging these KDE results. To explore the distribution nature of dS_n, the PDD type of dS_n is determined based on these KDE results. The Kolmogorov-Smirnov (K-S) test [57] is employed to test the PDD type of dS_n of each dH interval. The test results in Table 1 indicate that the hypothesis that the dS_n of each dH interval obeys the Weibull distribution is accepted ($P \gg 0.05$, $H = 0$) at the 95% confidence level. The Weibull distribution is defined as follows:

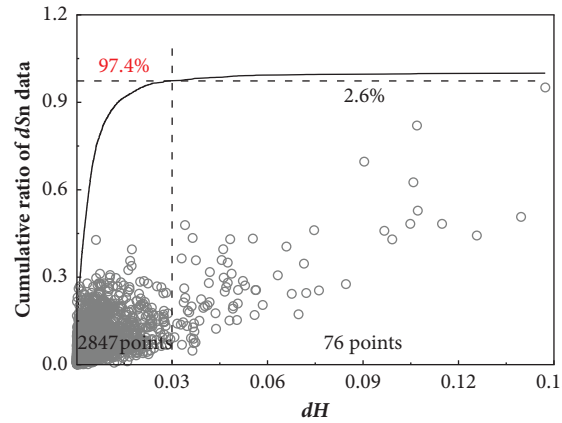

Figure 5: The cumulative ratio of dS_n data with increasing dH (LFH = 30 mm).

$$W(dS_n; \lambda, k) = \begin{cases} \frac{k}{\lambda}\left(\frac{dS_n}{\lambda}\right)^{k-1} \exp\left[-\left(\frac{dS_n}{\lambda}\right)\right]^k, & dS_n \geq 0, \\ 0, & dS_n < 0, \end{cases} \quad (16)$$

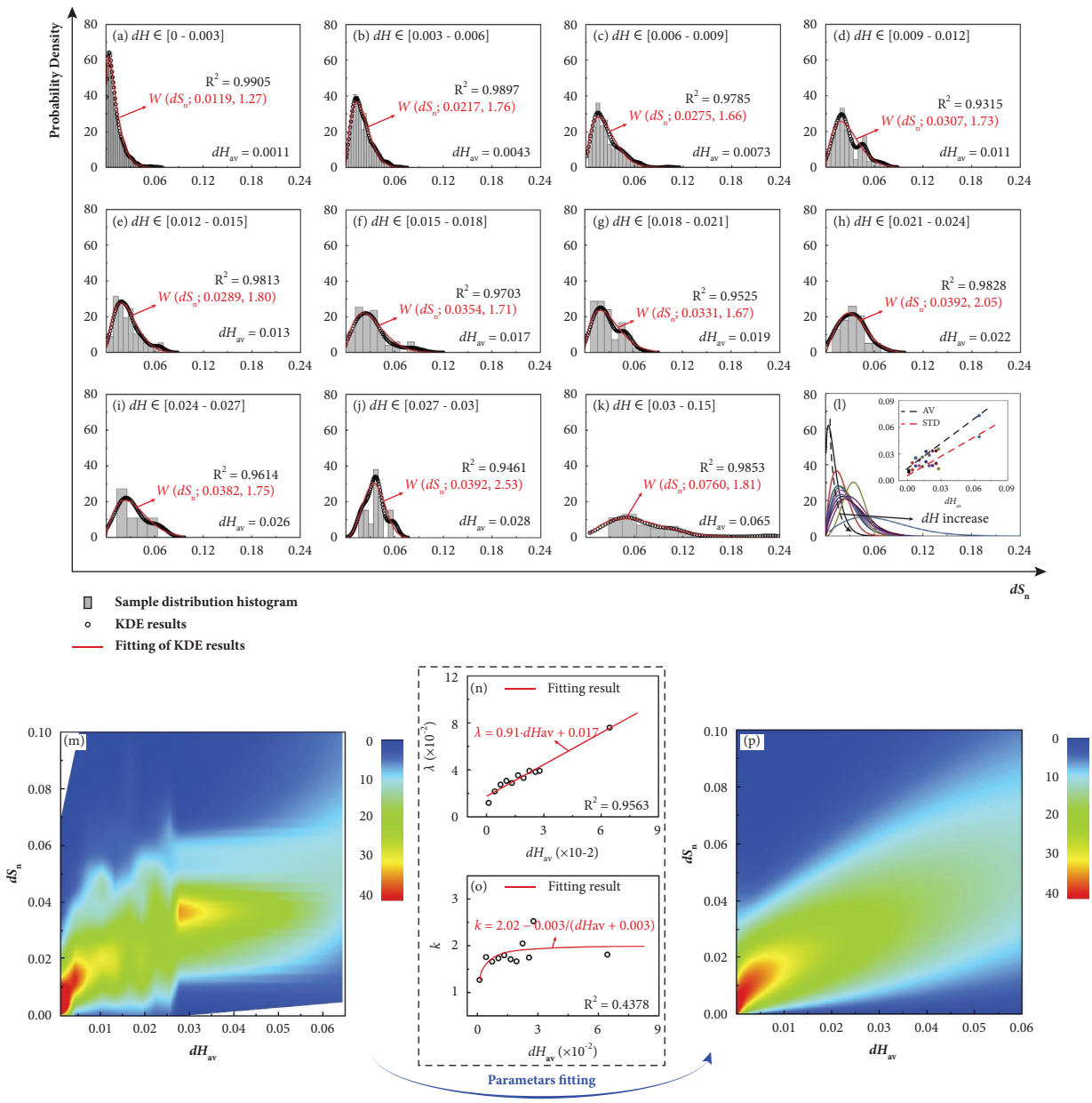

FIGURE 6: (a)–(k) histograms, KDE results, and fitted results of the PDD of all dH intervals, (l) linearly increasing average value (AV) and standard deviation (STD) of dS_n with the increasing dH_{av}, (m) two-dimensional KDE (real) PDD of dS_n, the fitting results of (n) λ and (o) k, and (p) the fitted two-dimensional PDD of dS_n (LFH = 30 mm).

where λ and k are the scale and shape parameters of the Weibull distribution.

The KDE results of dS_n are fitted using equation (16), as shown in Figures 6(a)–6(k). The fitting coefficient R^2 ranges from 0.9315 to 0.9905, indicating that the PDDs of dS_n can be accurately expressed by the Weibull distribution. As shown in Figure 6(l), as dH increases, both the average value AV and standard deviation STD of dS_n increase approximately linearly, which shows that the greater the SMFL field variation ratio, the greater the non-uniform corrosion degree. In addition, the distribution parameters λ and k of dS_n are approximately linearly and inverse proportionally increased with the increase of dH_{av}. Thus, they are fitted using linear and inverse proportional functions, respectively, as shown in Figures 6(n) and 6(o). Substituting the fitting results of λ and k into (16), the fitted PDD of dS_n shown in Figure 6(p) is obtained, which is similar to the KDE result shown in Figure 6(m) and shows the good adaptation of Weibull distribution in the determination of the PDD of dS_n.

Likewise, the PDDs of dS_n of other LFHs are obtained, as shown in Figure 7. The K-S test indicates that the PDDs of dS_n of different LFHs still obey the Weibull distribution. As shown in Figures 7(a) and 7(b), as dH_{av} increases, the parameter k shows an inversely proportional increase while the parameter λ evolves from a linear increase to an inversely proportional increase. The fitting result of the parameter λ has high accuracy, while that of k is not very good, which leads to some differences between the fitting results shown in Figures 7(c)–7(j) and the

Table 1: The *K-S* test of the hypothesis that dS_n obeys the Weibull distribution (95% confidence level).

dH interval	P	H
[0, 0.003]	0.9684	0
[0.003–0.006]	0.8664	0
[0.006–0.009]	0.7700	0
[0.009–0.012]	0.5893	0
[0.012–0.015]	0.9213	0
[0.015–0.018]	0.9771	0
[0.018–0.021]	0.9297	0
[0.021–0.024]	0.9570	0
[0.024–0.027]	0.9913	0
[0.027–0.03]	0.9990	0
[0.03–0.15]	0.7979	0

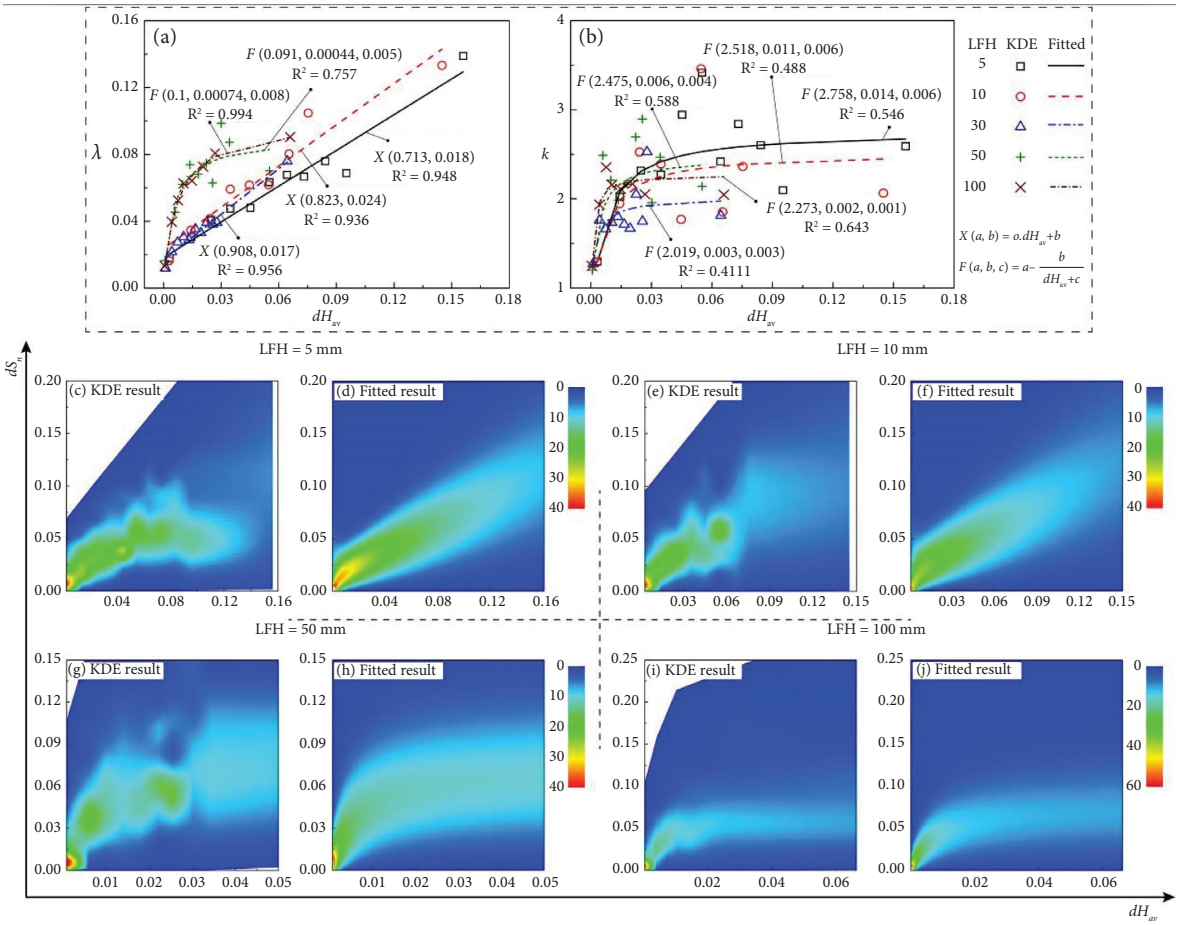

Figure 7: KDE and fitted results of distribution parameters (a) λ and (b) k, and (c)–(j) the two-dimensional KDE and fitted PDDs of dS_n with different LFHs.

KDE results. However, this difference becomes smaller with the decrease of dH_{av} and can be ignored in the small dH_{av} region that contains most of the data points.

4.2.3. SMFL-Based PDD of Index K. The PDD of K is also assessed using the KDE method. As shown in Figure 4(b), the sample points of K are distributed in the interval [0.25, 4.0], and the adjusted cross-sectional area ratio $K_{0.25} = K - 0.25$ is more suitable for the PDD estimation according to trial calculation. The K-S test results show that the hypothesis that the PDD of $K_{0.25}$ obeys the Gamma distribution is accepted at the 95% confidence level. The Gamma distribution is defined as follows:

$$G(K_{0.25}; a, b) = \begin{cases} \dfrac{1}{b^a \Gamma(a)} {K_{0.25}}^{a-1} \exp\left(-\dfrac{K_{0.25}}{b}\right), & K_{0.25} \geq 0, \\ 0, & K_{0.25} < 0, \end{cases} \tag{17}$$

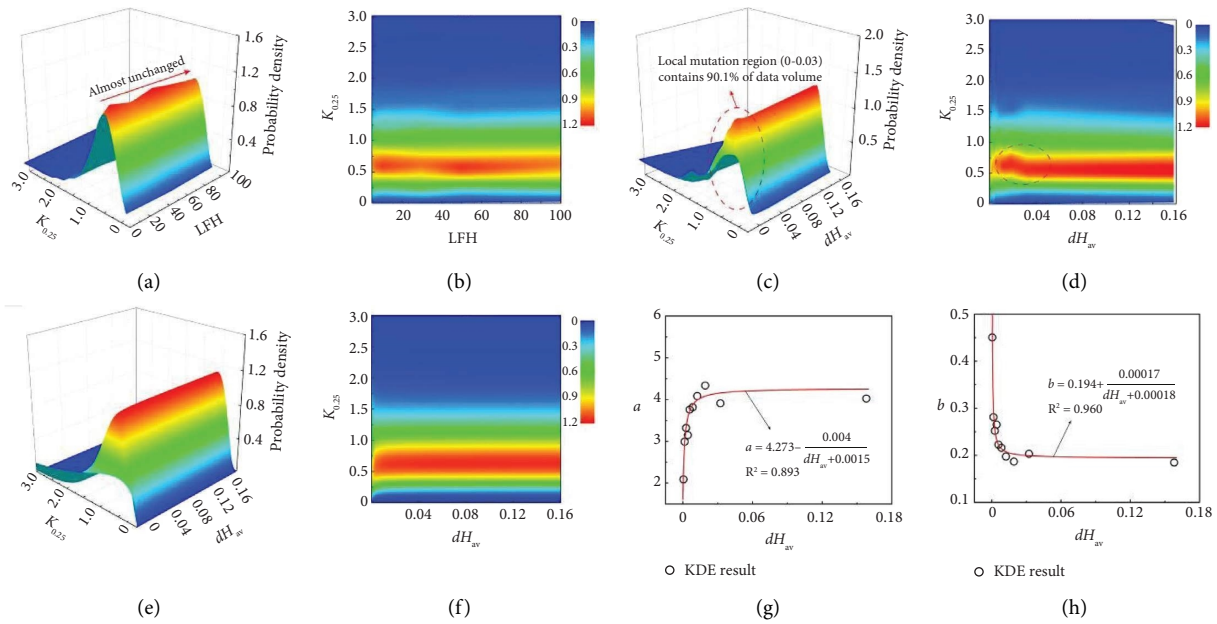

FIGURE 8: (a)–(f) KDE or fitted three-dimensional or two-dimensional PDDs of $K_{0.25}$ with different LFH or dH_{av}, and the distribution parameters (g) a and (h) b of PDDs of $K_{0.25}$.

where a and b are the shape and inverse scale parameters of the Gamma distribution.

As shown in Figures 8(a) and 8(b), the change of LFH has little effect on the shape and magnitude of the PDD of $K_{0.25}$. However, different from LFH, the KDE results in Figures 8(c) and 8(d) reveal the PDD of $K_{0.25}$ in the interval dH_{av} = [0,0.03] has a local mutation that contains 90.1% of the data volume, and thus the influence of dH need to be considered. As shown in Figures 8(g) and 8(h), the parameters a and b of $K_{0.25}$ are approximately inversely proportional to dH_{av} and can be well fitted by inverse proportional functions. Substituting the fitted results of a and b into equation (17), the fitted results of $K_{0.25}$ in Figures 8(e) and 8(f) are obtained and similar to the KDE results in Figures 8(c) and 8(d), which shows that it is appropriate to employ the Gamma distribution to determine the PDD of $K_{0.25}$.

4.3. The Application of SMFL-Based Assessment of S_{min} in Structural Reliability

4.3.1. The SMFL-Based PDD of S_{min}. Generally, RC structures have a 30 mm thick concrete cover, which leads to an LFH of no less than 30 mm. Taking LFH = 30 mm, then N values of dS_n and $K_{0.25}$ are randomly sampled according to equations (16) and (17), Figures 7 and 8, and the value of dH_{av}. Accordingly, N values of S_{min}/S_{avc} are calculated according to the N values of dS_n and $K_{0.25}$ and equation (8), based on which the PDD of S_{min}/S_{avc} is obtained, as shown in Figure 9. As dH_{av} increases, the PDD curves of S_{min}/S_{avc} become flatter and the probability density peak and its corresponding S_{min}/S_{avc} value decrease gradually, which indicates that a greater SMFL field variation degree

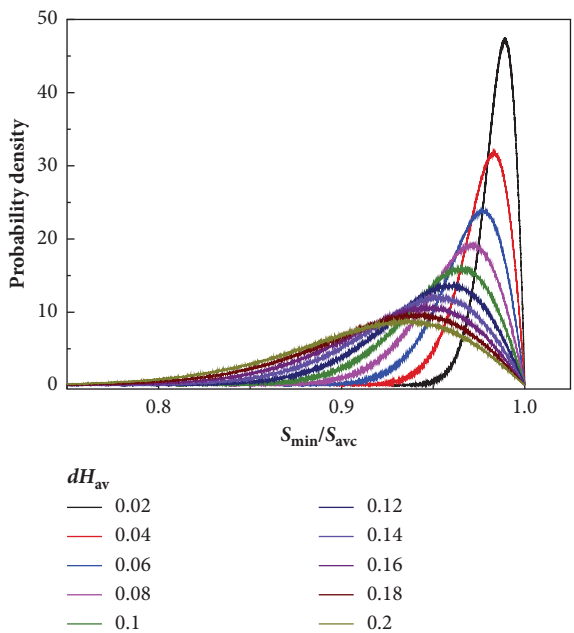

FIGURE 9: The PDDs of S_{min}/S_{avc} of different dH_{av} with LFH = 30 mm.

(increasing dH_{av}) means more non-uniform corrosion morphology and a smaller S_{min}. When S_{avc} is known, the PDD of S_{min} can be easily acquired, that is, the SMFL-based PDD assessment of S_{min} is implemented.

Since dH_{av} is obtained in the SMFL detection, the SMFL-based PDD of S_{min} is real, which has the same function as factor R but is free from adverse effects from rebar element length, corrosion current density, environment, and the prediction's cumulative error.

4.3.2. Feasibility of SMFL-Based Reliability Assessment of Non-Uniformly Corroded RC Beam. Since the SMFL-based PDD of $S_{\min}$ is obtained, the reliability assessment of RC beams with non-uniformity corrosion can be realized. However, there is a corrosion product layer and a concrete cover between the embedded rebars and the micro-magnetic sensors when detecting the SMFL field. Fortunately, the relative magnetic permeabilities of corrosion products and concrete are almost the same as that of air [41, 42, 51, 58]. Therefore, the PDD of $S_{\min}$ shown in Figure 9 is directly used in the reliability assessment of RC beams.

The MCS method detailed in Figure 1 is used for calculating β. As shown in Figure 10(a), a simply supported beam with a size of 5000 mm × 200 mm × 500 mm is reinforced by four hot-rolled rebars with a diameter of 14 mm, and the concrete cover is 30 mm thick. As shown in Figure 10(b), this corroded RC beam is assumed to bear uniformly distributed dead load G and sustained live load Q, and the rebars are non-uniformly corroded with an average cross-sectional corrosion degree $\eta_{\text{av}} = 1 - S_{\text{avc}}/S_0$ (S_0 is the cross-sectional area of the uncorroded rebar). The random sample of load, geometry, and material strength is according to Table 2. The clear span of the beam is divided into forty-eight 100 mm long beam segments, and the calculation of β is based on the bending resistance limit state with the assumption that the ends bent rebars are well-anchored.

Then, β of corroded RC beams with different η_{av} and dH_{av} values are calculated, as shown in Figure 10(c). For a corroded RC beam with a certain η_{av}, its β decreases with the increase of dH_{av}, which demonstrates the potential harm of non-uniform corrosion to the safety of RC beams. In addition, the fitting results of the distribution parameters λ, k, a, and b of dS_{n} and $K_{0.25}$ deviate from the actual values, whose effects on β need to be clarified. Therefore, the envelops and actual value curves of β shown in Figure 10(c) are obtained based on the fitting's 95% confidence levels and the actual values of parameters λ, k, a, and b listed in Table 3, respectively.

In Figure 10(c), the actual values of β with different dH_{av} all fall within these β envelopes. To quantify the exact effect of the fitting errors of λ, k, a, and b on β, the reliability index error E_β is defined as follows:

$$E_\beta = \left|\frac{\beta_{\text{U}} - \beta_{\text{L}}}{\beta_{\text{Ac}}}\right| \times 100\%, \tag{18}$$

where β_U and β_L are the upper and lower limits of the β envelop, respectively, and β_{Ac} is the corresponding actual value of β.

E_β with different η_{av} and dH_{av} are given in Figure 10(d). When $\eta_{\text{av}} < 0.4$, E_β of different dH_{av} do not exceed 3.2%, and when $\eta_{\text{av}} > 0.4$, E_β has an increasing trend and reaches a maximum value of 11%. Generally, the η_{av} of corroded RC beams is not very large, and thus these results indicate that the fitting errors of the parameters λ, k, a, and b will not lead to unacceptable errors in β.

In addition, the factor R-based [17, 18] and SMFL-based β curves of this corroded RC beam are compared in Figure 10(e). With the increase of η_{av}, the dH_{av} value corresponding to the intersection point of the R-based and the SMFL-based β curves gradually increases, which is consistent with the viewpoint of the factor R that the corrosion non-uniformity degree increases with the increase of η_{av} [17]. However, for a specific in-service RC structure, the relationship between corrosion non-uniformity degree and η_{av} is uncertain, which is a deficiency of R-based reliability assessment. For example, when $\eta_{\text{av}} > 0.5$, the R-based β corresponds to $dH_{\text{av}} > 0.2$, which in practice hardly occurs (see Figures 6–8). Of course, due to the limited original sample volume, the β with $dH_{\text{av}} > 0.2$ obtained based on the fitting results may not be exact. Overall, the R-based and SMFL-based β assessment methods have good consistency especially when η_{av} is small.

To reveal the effect of non-uniform corrosion on the reliability of RC beams intuitively, the failure probability growth ratio GR_p of a certain η_{av} is defined as follows:

$$\text{GR}_p = \frac{p_f(i)}{p_f(0)}, \tag{19}$$

where $p_f(i)$ and $p_f(0)$ are the failure probabilities of $dH_{\text{av}} = i$ and $dH_{\text{av}} = 0$, respectively.

As shown in Figure 10(f), the GR_p of different η_{av} increase exponentially with the increase of corrosion non-uniformity degree (increasing dH_{av}). When $\eta_{\text{av}} \le 0.25$, GR_p monotonically increases with the increase of η_{av}, and the maximum GR_p of different η_{av} range from 1.8 to 7.6 when $dH_{\text{av}} = 0.1$. These results show the exact adverse effect of non-uniform corrosion on the reliability of the corroded RC beam and are also generally consistent with the existing research results of the R-based or other methods [17, 18], indicating the feasibility of the SMFL-based reliability assessment of non-uniformly corroded RC beams.

4.3.3. Case Study of the Automatic Assessment of the Real Reliability of Corroded RC Beams Based on Detected SMFL Data. The true reliability of a specific corroded RC beam can be automatically assessed using its SMFL detection data and the MCS method. Taking the beam with a clear span of 5000 mm, a width of 300 mm, and a height of 1000 mm shown in Figure 2(a) as the case, it is assumed to bear dead load $G = 150$ kN/m and live load $Q = 50$ kN/m, and its clear span is divided into fifty 100 mm long beam segments, as shown in Figure 11(a). In Figure 11(b), S is the true cross-sectional area of the rebar obtained by the structural light scanning in Figure 2(b), and S_{avc} and $S_{\min}$ are the average and minimum cross-sectional areas of each beam segment calculated based on S. Since both ends of the rebars are well anchored, β of this beam is calculated based on the bending resistance limit state. The coefficients of variation and material strength distributions in Table 2 are used in the MCS calculation of β of this beam.

On the basis of the known S_{avc}, β of this beam can be calculated by SMFL-based or R-based method. As shown in Figure 11(c), the real dH of this beam is automatically calculated from the detected SMFL data, based on which the maximum value $dH_{\max}$ of each beam segment is accordingly obtained. Then, the PDDs of $S_{\min}$ of all beam segments are assessed by S_{avc} and $dH_{\max}$ refer to Figure 8. Accordingly, the SMFL-based β of 4.0 and failure probability p_f of 3.08×10^{-5} are acquired, as shown in Figure 11(d). According to the PDD of

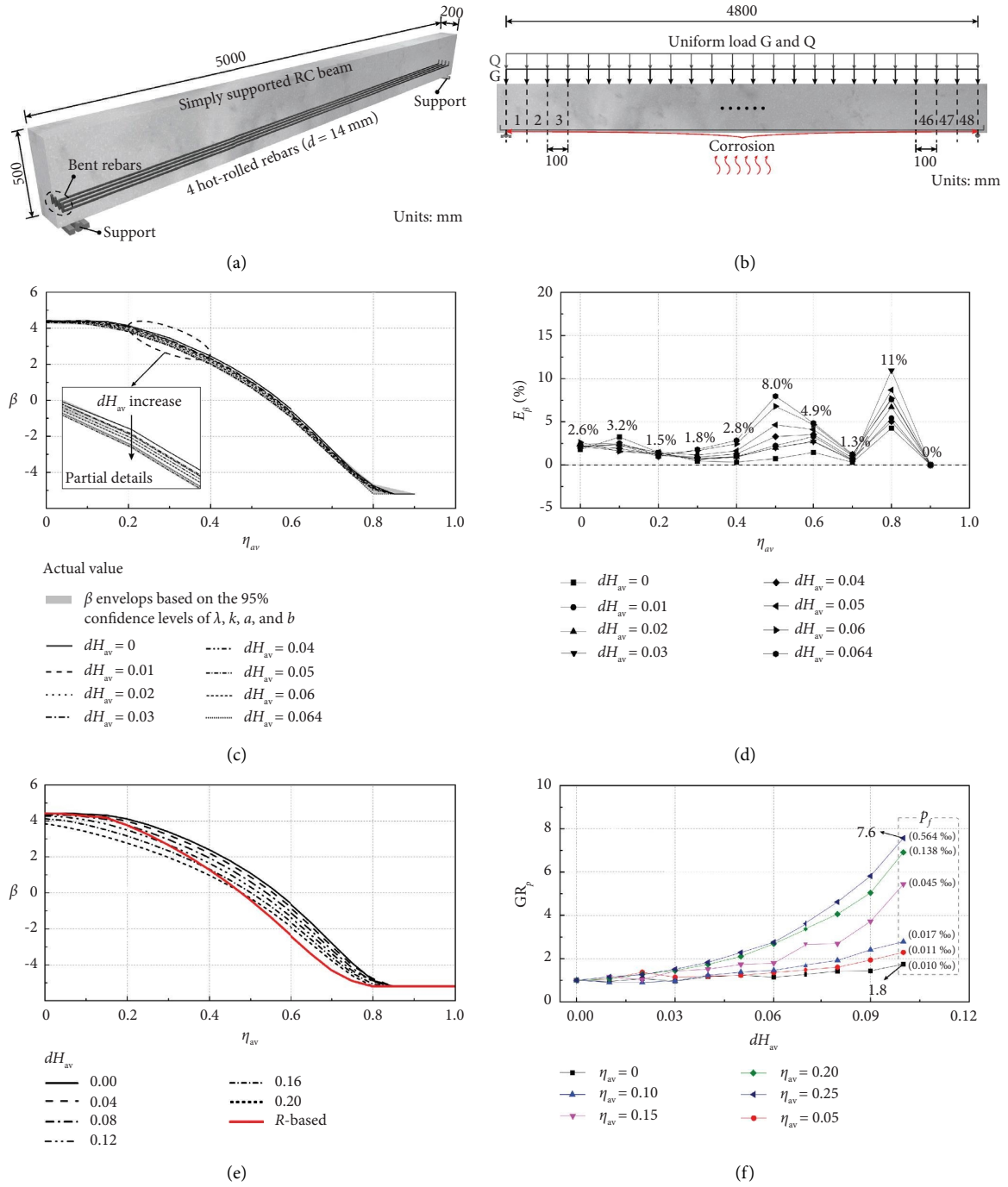

Figure 10: (a) Simply supported RC beam, (b) the load's distribution and beam segment division of the RC beam, (c) the envelops and actual curves of β with different η_{av} and dH_{av}, (d) reliability index error E_β caused by the fitting errors of distribution parameters λ, k, a, and b, (e) factor R-based and SMFL-based β curves, and (f) failure probability growth ratio GR_p for different η_{av} and dH_{av}.

Table 2: The distribution parameters of load, geometry, and material variables [17].

Variables	Mean	Coefficient of variation	Distribution
Dead load G (kN/m)	15	0.07	Normal
Sustained live load Q (kN/m)	6	0.29	Gumbel
Prism compressive strength f_c of concrete (MPa)	40	0.2	Normal
Yield strength f_y of rebars (MPa)	418	0.1	Log-normal
Effective cross-sectional depth h (mm)	463	0.02	Normal
Cross-sectional width b (mm)	200	0.02	Normal

Table 3: The 95% confidence levels ($X_{95\%}$) and actual values (X_{Ac}) of parameters λ, k, a, and b with different dH_{av} (LFH = 30 mm).

dH_{av}	$\lambda_{95\%}$ ($\times 10^{-2}$)	λ_{Ac}	$k_{95\%}$	k_{Ac}	$a_{95\%}$	a_{Ac}	$b_{95\%}$	b_{Ac}
0	[0.85, 0.88]	0.86	[1.09, 1.13]	1.11	[1.59, 1.72]	1.66	[0.51, 0.56]	0.53
0.01	[3.02, 3.11]	3.05	[1.66, 1.79]	1.72	[3.81, 4.04]	3.93	[0.20, 0.22]	0.21
0.02	[3.43, 3.48]	3.44	[1.70, 1.79]	1.74	[4.19, 4.13]	4.31	[0.18, 0.20]	0.19
0.03	[4.14, 4.25]	4.2	[2.38, 2.59]	2.48	[3.86, 4.11]	3.99	[0.19, 0.21]	0.20
0.04	[5.15, 5.25]	5.19	[2.20, 2.38]	2.29	[3.79, 4.04]	3.92	[0.19, 0.21]	0.20
0.05	[6.15, 6.25]	6.18	[2.02, 2.17]	2.09	[3.80, 4.05]	3.93	[0.19, 0.21]	0.20
0.06	[7.16, 7.25]	7.17	[1.84, 1.96]	1.90	[3.81, 4.06]	3.94	[0.19, 0.21]	0.20
0.064	[7.61, 7.69]	7.64	[1.76, 1.86]	1.81	[3.82, 4.06]	3.94	[0.19, 0.21]	0.20

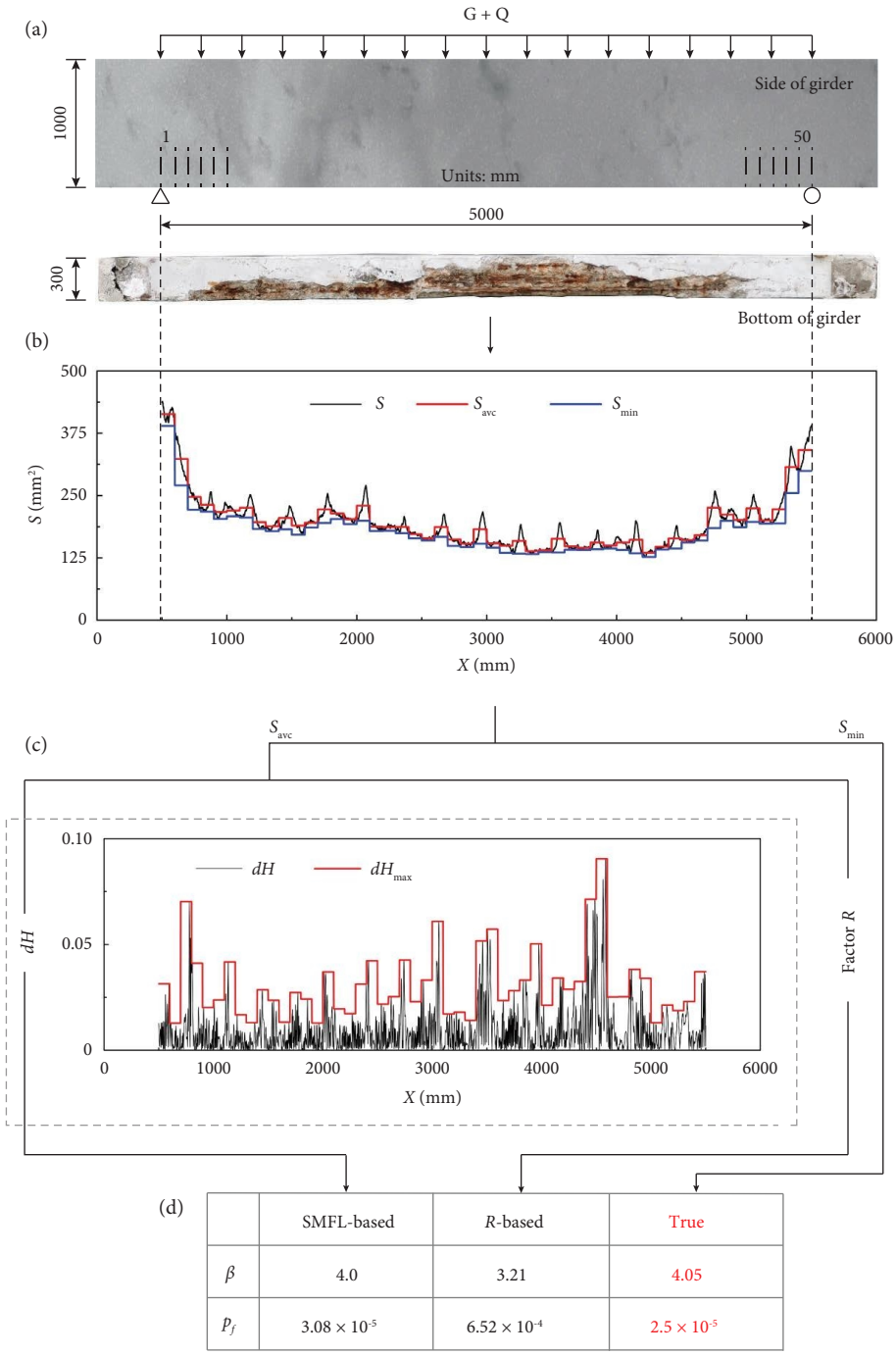

Figure 11: (a) The geometric dimensions of a specific corroded beam, (b) the cross-sectional area S of the corroded rebars of this beam, (c) the true dH of this beam, and (d) β and p_f calculated by different methods.

factor R [17], the PDDs of $S_{\min}$ of all beam segments are obtained, based on which the R-based β of 3.21 and p_f of 6.52×10^{-4} are acquired, as shown in Figure 11(d).

Based on the real $S_{\min}$ value in Figure 11(b), the true β of 4.05 and p_f of 2.5×10^{-5} of this beam are acquired, as shown in Figure 11(d). In contrast, the SMFL-based β and p_f are close to the truth, with a reliability error of only 1.2% and a failure probability error of 23.2%. However, there is a big difference between the R-based β and p_f and the truth, with a reliability error of up to 20.7% and a failure probability error of an astonishing 64200%. To avoid this error, one effective approach is to establish a PDD model of factor R-based on data from those naturally corroded girders shown in Figure 2(a). However, the process of establishing such PDD model of factor is arduous and labor-intensive. This is precisely why we have developed this non-destructive SMFL-based method as an alternative to the R-based method for assessing the corrosion non-uniformity and reliability of corroded RC structures.

This case study demonstrates the high accuracy of SMFL-based reliability assessment of corroded RC structures, in which the reliability misestimation due to non-uniform corrosion is greatly reduced. In addition, the SMFL-based reliability assessment of a specific RC structure can be automatically realized using the MCS method once its SMFL data is detected. Therefore, the SMFL-based reliability assessment method has great potential in practical applications.

5. Conclusions

In this study, the SMFL-based assessment of the minimum cross-sectional area of corroded rebar is realized, based on which the reliability assessment case study of a non-uniformly corroded RC beam is carried out. The following conclusions can be drawn:

(1) The value of the SMFL field variation ratio dH is an effective index to characterize the corrosion non-uniformity degree dS_n of rebar quantitatively.

(2) At the 95% confidence level, the corrosion non-uniformity degree dS_n and the cross-sectional area ratio $K_{0.25}$ obey the Weibull distribution and Gamma distribution with distribution parameters linearly or inversely proportionally correlated to dH, respectively.

(3) For non-uniformly corroded RC beam with a certain average corrosion degree η_{av} and SMFL field variation ratio dH, the rebar's minimum cross-sectional area $S_{\min}$ can be determined based on η_{av} and the PDDs of dS_n and $K_{0.25}$ that depend on dH. The reliability assessment example of a non-uniformly corroded RC beam indicates that the increase of dH means a substantial increase (up to 180%–760%) in the failure probability.

(4) A novel SMFL-based method with better adaptability to the automatic reliability assessment of specific in-service corroded RC beams is developed. A real case shows that this SMFL-based method can reduce the reliability assessment error from 20.7% of the existing R-based method to a very low level of 1.2%.

Some aspects, including the weakened strength of corroded rebar and the effects of stress and stirrups on the SMFL field, have not been considered in this study temporarily. In addition, the effects of concrete cover and corrosion products on this proposed SMFL-based assessment method of corrosion non-uniformity of rebars and reliability of corroded RC structures also need to be deeply explored and solved. Related issues will be discussed in detail in our future work.

Nomenclature

a: Parameter of gamma distribution
AAv: Adjacent-average
b: Parameter of gamma distribution
d: Depth of V- shape corrosion
dH: SMFL field variation ratio
dH_{av}: Average value of dH
$dH_{\max}$: Maximum value of dH
dS_n: Corrosion non-uniformity degree
E_β: Reliability index error
G: Dead load
GR_p: Failure probability growth ratio
h: Bandwidth of kernel density estimation
h_{opt}: Optimal h
$\mathbf{H_e}$: Geomagnetic field
H_{ex}: x component of $\mathbf{H_e}$
H_{ey}: y component of $\mathbf{H_e}$
H_{ez}: z component of $\mathbf{H_e}$
$\mathbf{H}$: SMFL field strength
H_x: x component of $\mathbf{H}$
H_z: y component of $\mathbf{H}$
k: Shape parameter of Weibull distribution
K: Cross-sectional area ratio
$K_{0.25}$: Adjusted cross-sectional area ratio
$K(\cdot)$: Kernel function
KDE: Kernel density estimation
LFH: Lift-off height of SMFL scanning
m: Parameter of SG or AAv smoothing
M_S: Applied bending moment
MCS: Monte Carlo simulation
MISE: Mean integral square error
M_u: Ultimate flexural bearing capacity
n: Parameter of SG smoothing
N: Times of Monte Carlo simulation
$\text{N} - \Delta H_{\text{SA}}$: Quantitative SMFL variation degree
p_f: Failure probability
PDD: Probability density distribution
Q: Live load
r: Radius of the rebar
R: Cross-sectional area spatial heterogeneity factor
RC: Reinforced concrete
S: Cross-sectional area of corroded rebar
S_{avc}: Average cross-sectional area
$S_{\max}$: Rebar's maximum cross-sectional area
$S_{\min}$: Rebar's minimum cross-sectional area
S_{Am}: SMFL variation amplitude
S_0: Cross-sectional area of uncorroded rebar
SG: Savitzky-golay

SMFL: Self-magnetic flux leakage
$\mathbf{V}$: Magnetization vector
V_x: x component of $\mathbf{V}$
V_y: y component of $\mathbf{V}$
V_z: z component of $\mathbf{V}$
$\mathbf{V_h}$: Geomagnetic field-induced magnetization vector
$\mathbf{V_r}$: Residual magnetization vector
x: x-axis coordinate
y: y-axis coordinate
z: z-axis coordinate
w: Half-width of V- shape corrosion
β: Reliability index
ρ: Symbol of magnetic charge
λ: Scale parameter of Weibull distribution
η_{av}: Average cross-sectional corrosion degree of rebar
μ_0: Vacuum magnetic permeability
μ_{ra}: Relative magnetic permeability of air
μ_{rs}: Relative magnetic permeability of rebar
ΔH_{SS}: Real SMFL field variation
ΔH_{SA}: Simulated SMFL field variation.

Data Availability

The data can be obtained from the corresponding author upon request.

Conflicts of Interest

The authors declare that they have no conflicts of interest.

Acknowledgments

The authors sincerely thank Ruilin Wang, the doctoral candidate of the Department of structural engineering of Tongji University, for his help in writing the calculation codes. This research was funded by the National Natural Science Foundation of China (51878486) and the Program of Shanghai Science and Technology Committee (22dz1203603).

References

[1] C. Jiang, H. Ding, X. L. Gu, and W. P. Zhang, "Failure mode-based calculation method for bending bearing capacities of normal cross-sections of corroded reinforced concrete beams," *Engineering Structures*, vol. 258, Article ID 114113, 2022.

[2] C. Jiang, H. Ding, X. L. Gu, and W. P. Zhang, "Calibration analysis of calculation formulas for shear capacities of corroded RC beams," *Engineering Structures*, vol. 286, Article ID 116090, 2023.

[3] U. M. Angst, "Predicting the time to corrosion initiation in reinforced concrete structures exposed to chlorides," *Cement and Concrete Research*, vol. 115, pp. 559–567, 2019.

[4] Y. Zhou, B. Gencturk, K. Willam, and A. Attar, "Carbonation-induced and chloride-induced corrosion in reinforced concrete structures," *Journal of Materials in Civil Engineering*, vol. 27, no. 9, Article ID 04014245, 2015.

[5] K. X. Liao, Y. P. Zhang, W. P. Zhang, Y. Wang, and R. L. Zhang, "Modeling constitutive relationship of sulfate-attacked concrete," *Construction and Building Materials*, vol. 260, Article ID 119902, 2020.

[6] K. J. Zhang, J. Z. Xiao, and Q. T. Zhang, "Time-dependent reliability analysis of recycled aggregate concrete cover cracking induced by reinforcement corrosion," *Journal of Building Engineering*, vol. 39, Article ID 102320, 2021.

[7] J. Bojórquez, S. Ponce, S. E. Ruiz et al., "Structural reliability of reinforced concrete buildings under earthquakes and corrosion effects," *Engineering Structures*, vol. 237, Article ID 112161, 2021.

[8] D. Veneziano, C. A. Cornell, and M. Grigoriu, "Vector-process models for system reliability," *Journal of the Engineering Mechanics Division*, vol. 103, no. 3, pp. 441–460, 1977.

[9] D. M. Frangopol, K. Y. Lin, and A. C. Estes, "Reliability of reinforced concrete girders under corrosion attack," *Journal of Structural Engineering*, vol. 123, no. 3, pp. 286–297, 1997.

[10] A. Der Kiureghian, H. Z. Lin, and S. J. Hwang, "Second-order reliability approximations," *Journal of Engineering Mechanics*, vol. 113, no. 8, pp. 1208–1225, 1987.

[11] M. Akiyama, D. M. Frangopol, and H. Ishibashi, "Toward life-cycle reliability-risk-and resilience-based design and assessment of bridges and bridge networks under independent and interacting hazards: emphasis on earthquake, tsunami and corrosion," *Structure and Infrastructure Engineering*, vol. 16, no. 1, pp. 26–50, 2020.

[12] J. Li and J. B. Chen, *Stochastic Dynamics of Structures*, John Wiley & Sons, New York, NY, USA, 2009.

[13] H. Y. Guo, Y. Dong, and P. Gardoni, "Efficient subset simulation for rare-event integrating point-evolution kernel density and adaptive polynomial chaos kriging," *Mechanical Systems and Signal Processing*, vol. 169, Article ID 108762, 2022.

[14] M. G. Stewart and A. Al-Harthy, "Pitting corrosion and structural reliability of corroding RC structures: experimental data and probabilistic analysis," *Reliability Engineering and System Safety*, vol. 93, no. 3, pp. 373–382, 2008.

[15] M. Y. Zhang, H. J. Song, S. Lim, M. Akiyama, and D. M. Frangopol, "Reliability estimation of corroded RC structures based on spatial variability using experimental evidence, probabilistic analysis and finite element method," *Engineering Structures*, vol. 192, pp. 30–52, 2019.

[16] H. Hamidane, A. Chateauneuf, A. Messabhia, and A. Ababneh, "Reliability analysis of corrosion initiation in reinforced concrete structures subjected to chlorides in presence of epistemic uncertainties," *Structural Safety*, vol. 86, Article ID 101976, 2020.

[17] W. P. Zhang, B. B. Zhou, X. L. Gu, and H. Dai, "Probability distribution model for cross-sectional area of corroded reinforcing steel bars," *Journal of Materials in Civil Engineering*, vol. 26, no. 5, pp. 822–832, 2014.

[18] X. L. Gu, H. Y. Guo, B. B. Zhou, W. P. Zhang, and C. Jiang, "Corrosion non-uniformity of steel bars and reliability of corroded RC beams," *Engineering Structures*, vol. 167, pp. 188–202, 2018.

[19] X. G. Liu, W. P. Zhang, X. L. Gu, and Z. W. Ye, "Probability distribution model of stress impact factor for corrosion pits of high-strength prestressing wires," *Engineering Structures*, vol. 230, Article ID 111686, 2021.

[20] M. Otieno, H. Beushausen, and M. Alexander, "Prediction of corrosion rate in reinforced concrete structures–a critical review and preliminary results," *Materials and Corrosion*, vol. 63, no. 9, pp. 777–790, 2012.

[21] Y. C. Ou, Y. T. T. Susanto, and H. Roh, "Tensile behavior of naturally and artificially corroded steel bars," *Construction and Building Materials*, vol. 103, pp. 93–104, 2016.

[22] C. Chalhoub, R. François, and M. Carcasses, "Critical chloride threshold values as a function of cement type and steel surface condition," *Cement and Concrete Research*, vol. 134, Article ID 106086, 2020.

[23] C. Song, C. Jiang, X. L. Gu, Q. Zhang, and W. P. Zhang, "Calibration analysis of chloride binding capacity for cement-based materials under various exposure conditions," *Construction and Building Materials*, vol. 314, Article ID 125588, 2022.

[24] C. Jiang, C. Song, X. L. Gu, Q. Zhang, and W. P. Zhang, "Modeling electrochemical chloride extraction process in cement-based materials considering coupled multi-ion transports and thermodynamic equilibriums," *Journal of Cleaner Production*, vol. 401, Article ID 136778, 2023.

[25] C. B. Cheah, L. E. Tan, and M. Ramli, "The engineering properties and microstructure of sodium carbonate activated fly ash/slag blended mortars with silica fume," *Composites Part B: Engineering*, vol. 160, pp. 558–572, 2019.

[26] Q. W. Qiu, "A state-of-the-art review on the carbonation process in cementitious materials: fundamentals and characterization techniques," *Construction and Building Materials*, vol. 247, Article ID 118503, 2020.

[27] C. Jiang, X. L. Gu, Q. H. Huang, and W. P. Zhang, "Carbonation depth predictions in concrete bridges under changing climate conditions and increasing traffic loads," *Cement and Concrete Composites*, vol. 93, pp. 140–154, 2018.

[28] C. Jiang, Q. H. Huang, X. L. Gu, and W. P. Zhang, "Modeling the effects of fatigue damage on concrete carbonation," *Construction and Building Materials*, vol. 191, pp. 942–962, 2018.

[29] V. Carević and I. Ignjatović, "Influence of loading cracks on the carbonation resistance of RC elements," *Construction and Building Materials*, vol. 227, Article ID 116583, 2019.

[30] C. Jiang, Q. H. Huang, X. L. Gu, and W. P. Zhang, "Experimental investigation on carbonation in fatigue-damaged concrete," *Cement and Concrete Research*, vol. 99, pp. 38–52, 2017.

[31] H. G. Min and W. P. Zhang, "Effects of coupled heat and moisture and load damage on chloride transport in concrete," *Magazine of Concrete Research*, vol. 74, no. 13, pp. 659–671, 2022.

[32] J. Y. Chen, W. P. Zhang, Z. J. Tang, and Q. H. Huang, "Experimental and numerical investigation of chloride-induced reinforcement corrosion and mortar cover cracking," *Cement and Concrete Composites*, vol. 111, Article ID 103620, 2020.

[33] J. Alam, L. A. C. Neves, H. Zhang, and D. Dias-da-Costa, "Assessment of remaining service life of deteriorated concrete bridges under imprecise probabilistic information," *Mechanical Systems and Signal Processing*, vol. 167, Article ID 108565, 2022.

[34] A. Kamariotis, E. Chatzi, and D. Straub, "Value of information from vibration-based structural health monitoring extracted via Bayesian model updating," *Mechanical Systems and Signal Processing*, vol. 166, Article ID 108465, 2022.

[35] H. Zhang, H. X. Li, J. T. Zhou, K. Tong, and R. C. Xia, "A multi-dimensional evaluation of wire breakage in bridge cable based on self-magnetic flux leakage signals," *Journal of Magnetism and Magnetic Materials*, vol. 566, Article ID 170321, 2023.

[36] K. Tong, J. T. Zhou, R. Q. Zhao, W. X. Hu, Y. H. Qu, and C. S. Cheng, "Experimental study on rebar stress measurement based on force-magnetic coupling under excited magnetic field," *Measurement*, vol. 189, Article ID 110620, 2022.

[37] H. Zhang, X. T. Ma, H. J. Jiang, K. Tong, Y. Zheng, and J. T. Zhou, "Grading evaluation of overall corrosion degree of corroded RC beams via SMFL technique," *Structural Control and Health Monitoring*, vol. 2023, Article ID 6672823, 23 pages, 2023.

[38] D. Yang, J. Qiu, H. Di, S. Zhao, J. Zhou, and F. Yang, "Quantitative evaluation of corrosion degrees of steel bars based on self-magnetic flux leakage," *Metals*, vol. 9, p. 952, 2019.

[39] H. Zhang, J. B. Qi, Y. Zheng, J. T. Zhou, and J. L. Qiu, "Characterization and grading assessment of rebar corrosion in loaded RC beams via SMFL technology," *Construction and Building Materials*, vol. 411, Article ID 134484, 2024.

[40] J. H. Huang, Z. Dong, C. Q. Fu et al., "Evaluation of non-uniform corrosion of steel in concrete based on two-yoke magnetic sensor," *Journal of Materials in Civil Engineering*, vol. 34, no. 9, Article ID 04022204, 2022.

[41] C. Q. Fu, J. H. Huang, Z. Dong, W. J. Yan, and X. L. Gu, "Experimental and numerical study of an electromagnetic sensor for non-destructive evaluation of steel corrosion in concrete," *Sensors and Actuators A: Physical*, vol. 315, Article ID 112371, 2020.

[42] J. R. Zhang, C. Liu, M. Sun, and Z. J. Li, "An innovative corrosion evaluation technique for reinforced concrete structures using magnetic sensors," *Construction and Building Materials*, vol. 135, pp. 68–75, 2017.

[43] J. L. Qiu, J. T. Zhou, S. Y. Zhao, H. Zhang, and L. Liao, "Statistical quantitative evaluation of bending strength of corroded RC beams via SMFL technique," *Engineering Structures*, vol. 209, Article ID 110168, 2020.

[44] J. L. Qiu, H. Zhang, J. T. Zhou, and W. P. Zhang, "An SMFL-based non-destructive quantification method for the localized corrosion cross-sectional area of rebar," *Corrosion Science*, vol. 192, Article ID 109793, 2021.

[45] R. C. Xia, H. Zhang, J. T. Zhou, L. Liao, Z. Y. Zhang, and F. X. Yang, "Probability evaluation method of cable corrosion degree based on self-magnetic flux leakage," *Journal of Magnetism and Magnetic Materials*, vol. 522, Article ID 167544, 2021.

[46] S. Srivaranun, M. Akiyama, P. Bocchini et al., "Effect of the interaction of corrosion pits among multiple tensile rebars on the reliability of RC structures: experimental and numerical investigation," *Structural Safety*, vol. 93, Article ID 102115, 2021.

[47] Y. Wang, C. Liu, Y. Wang, Q. Li, and B. Yan, "Semi-empirical prediction model of chloride-induced corrosion rate in uncracked reinforced concrete exposed to a marine environment," *Electrochimica Acta*, vol. 331, Article ID 135376, 2020.

[48] J. E. Ramón, J. M. Gandía-Romero, R. Bataller, M. Alcañiz, M. Valcuende, and J. Soto, "Potential step voltammetry: an approach to corrosion rate measurement of reinforcements in concrete," *Cement and Concrete Composites*, vol. 110, Article ID 103590, 2020.

[49] V. Talakokula, S. Bhalla, R. J. Ball et al., "Diagnosis of carbonation induced corrosion initiation and progression in reinforced concrete structures using piezo-impedance transducers," *Sensors and Actuators A: Physical*, vol. 242, pp. 79–91, 2016.

[50] J. L. Qiu, H. Zhang, J. T. Zhou, H. Ma, and L. Liao, "Experimental analysis of the correlation between bending strength and SMFL of corroded RC beams," *Construction and Building Materials*, vol. 214, pp. 594–605, 2019.

[51] J. Qiu, W. Zhang, and Y. Jing, "Quantitative linear correlation between self-magnetic flux leakage field variation and corrosion unevenness of corroded rebars," *Measurement*, vol. 218, Article ID 113173, 2023.
[52] P. Zhao, G. Xu, Q. Wang, and G. J. Tang, "Influence of sustained load on corrosion characteristics of reinforced concrete beams under galvanostatic accelerated corrosion," *Construction and Building Materials*, vol. 215, pp. 30–42, 2019.
[53] A. Savitzky and M. J. E. Golay, "Smoothing and differentiation of data by simplified least squares procedures," *Analytical Chemistry*, vol. 36, no. 8, pp. 1627–1639, 1964.
[54] J. S. Simonoff, *Smoothing Methods in Statistics*, Springer Science & Business Media, Berlin, Germany, 2012.
[55] E. Parzen, "On estimation of a probability density function and mode," *The Annals of Mathematical Statistics*, vol. 33, no. 3, pp. 1065–1076, 1962.
[56] M. Rosenblatt, "Remarks on some nonparametric estimates of a density function," *The Annals of Mathematical Statistics*, vol. 27, no. 3, pp. 832–837, 1956.
[57] W. J. Conover, *Practical Nonparametric Statistics*, John Wiley & Sons, New York, NY, USA, 1999.
[58] Z. Li, Z. Jin, T. Zhao et al., "Use of a novel electro-magnetic apparatus to monitor corrosion of reinforced bar in concrete," *Sensors and Actuators A: Physical*, vol. 286, pp. 14–27, 2019.